The Double Peak in Upwelling and Heating in the Tropical Lower Stratosphere

ALISON MING, PETER HITCHCOCK, AND PETER HAYNES

Department of Applied Mathematics and Theoretical Physics, University of Cambridge, Cambridge, United Kingdom

(Manuscript received 3 September 2015, in final form 8 February 2016)

ABSTRACT

The processes responsible for double-peak latitudinal structures in the time-averaged tropical lower-stratospheric upwelling, centered near 70 hPa and 20°N/S, previously noted in ERA-Interim and other reanalysis and model datasets, are considered. It is demonstrated that the structure of the wave force resolved by ERA-Interim consistently balances the angular momentum transport associated with the double peak. Analysis of the corresponding structures in diabatic heating rates from ERA-Interim indicates that the peaks arise predominantly from the meridional structure in ozone concentrations and the associated absorption of both shortwave and longwave radiation. Additional smaller contributions arise from local absorption of longwave radiation emitted from the relatively warm layers above and below, as well as from cloud-related radiative effects and nonradiative diabatic heating. The temperature at 70 hPa is slightly higher near 20°N/S than at the equator, opposite of what would be expected if the latitudinal structure in radiative heating were associated with local relaxation. It is proposed on the basis of this analysis that the primary cause of the peaks in upwelling is the externally imposed (i.e., nonrelaxational) part of the radiative heating field. The dynamical plausibility of this hypothesis is investigated in a companion paper.

1. Introduction

The Brewer–Dobson circulation is recognized as an important component of the chemistry–climate system. In the lower and middle stratosphere, the circulation is upward at low latitudes and downward at high latitudes and, therefore, controls the rate at which chemical species with tropospheric sources are taken into the stratosphere. Correspondingly, it also controls the rate at which species with sources in the stratosphere and mesosphere are taken into to the troposphere. Brewer's important paper (Brewer 1949), deducing the existence of a global-scale circulation on the basis of a small number of extratropical water vapor measurements, noted that if such a circulation existed then an explanation would be needed for the angular momentum balance, but the paper did not attempt to provide such an explanation.

Subsequent theoretical and modeling studies have established the steady component of the Brewer–Dobson circulation (i.e., what would be observed from a multiyear average) as a wave-driven circulation in which the Coriolis force associated with poleward flow is balanced by the wave force due to dissipating Rossby waves and gravity waves (e.g., Plumb 2002; Butchart 2014). The relation between the wave force and the circulation is encapsulated in the "downward control" principle derived by Haynes et al. (1991), who considered the zonally symmetric response of a radiatively damped atmosphere to a prescribed zonally symmetric force. The upwelling or downwelling through a certain level is controlled purely by the distribution of the wave force above that level. In this steady zonally symmetric regime, an applied heating will not drive a circulation—the response to such a heating is simply an adjustment in temperatures such that the applied heating is balanced by a change in the longwave radiative heating.

While this analysis, based on zonally symmetric dynamics, makes the important point that there cannot be a circulation without a wave force (or a systematic change in circulation without a change in wave force), it does not account for the possibility that the wave force itself may change as part of the response to an applied heating and that such a change will correspondingly drive a steady meridional circulation. A well-known example of this is the response of the middle atmosphere to increased greenhouse gases—the direct forcing of the system is a heating but this results in a change in the

Corresponding author address: Alison Ming, DAMTP, University of Cambridge, Centre for Mathematical Sciences, Wilberforce Road, Cambridge CB3 0WA, United Kingdom.
E-mail: a.ming@damtp.cam.ac.uk

DOI: 10.1175/JAS-D-15-0293.1

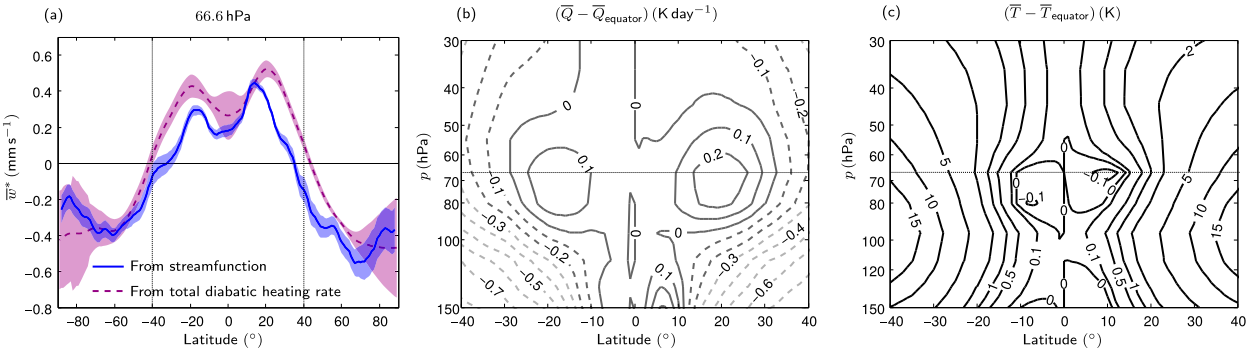

FIG. 1. Zonally averaged ERA-Interim data from 1991 to 2010. (a) Plots of the mean vertical residual velocity (mm s^{-1}) at 66.6 hPa estimated from the streamfunction and from the diabatic heating rates. The 95% confidence intervals are calculated from an adjusted Student's t test. (b) Diabatic heating rate (K day^{-1}) expressed as difference from the value at the equator to emphasize the horizontal gradients (since strong vertical gradients are present). (c) Temperature difference (K) from the temperature at the equator. Vertical dotted lines in (a) and horizontal dotted lines in (b) and (c) are intended as guides for the latitude range 40°N–S and the pressure level of 66.6 hPa, respectively.

wave force and hence a change in the meridional circulation (e.g., Butchart et al. 2010a; Garcia and Randel 2008; Shepherd and McLandress 2011; Butchart and Scaife 2001). The decadal changes in meridional circulation due to the ozone hole might provide another example.

This paper is motivated by the low-latitude structure of the upwelling meridional circulation in observations and certain model simulations. A feature of the upwelling velocity is a double-peak structure with two local maxima at about 20°N/S and 70 hPa observed in the ERA-Interim dataset as shown in Fig. 1a and by Seviour et al. (2012), as well as in various other reanalysis datasets (Abalos et al. 2015) and coupled chemistry–climate models [Fig. 4.9 in chapter 4 of Butchart et al. (2010b) and Fig. 3 of Butchart et al. (2006)]. Similar double peaks are present in the diabatic heating rates at these levels in ERA-Interim (Fueglistaler et al. 2009) as shown in Fig. 1b.

In contrast, the temperature does not exhibit the same latitudinal structure across the equator, as shown in Fig. 1c. The difference from the equatorial value at 20°N/S is less than 1 K and furthermore the temperature increases away from the equator. A local relaxational model for the temperature dependence of the radiative heating would therefore imply that there should be less radiative heating at 20°N/S relative to the equator rather than what is observed, which is greater radiative heating. This suggests that some part of the radiative heating might be externally imposed. We will return to discuss what "externally imposed" actually means in more depth in section 5.

The motivation for the work reported in this paper and in a companion paper (Ming et al. 2016) is to understand the cause of the double peak in upwelling. To establish the cause, it is necessary to consider together both the radiative balance and the angular momentum balance. Certainly to achieve the required angular momentum balance, it is necessary that the westward wave force that drives poleward flow and hence low-latitude upwelling and higher-latitude downwelling is suitably confined away from the equator. This confinement might occur in the absence of any external radiative heating—it might, for example, arise simply from the behavior of planetary- and synoptic-scale Rossby waves propagating from the extratropics. On the other hand, it might be that an externally imposed radiative heating plays an active role in determining the structure of the wave force.

The structure of the paper is as follows. Section 2 describes the data and the offline radiation codes used in the remainder of the paper. In section 3, we review the structure of the upwelling, temperature, and diabatic heating in ERA-Interim data and show that the wave force is indeed consistent with the double-peak structure in upwelling. Then in section 4, we consider in more detail how the pattern in diabatic heating rates seen in ERA-Interim data arises, first by considering contributions from individual processes to the total diabatic heating rate and then using an offline radiative code to gain further insight into how the clear-sky heating is determined by the concentrations of different radiatively active constituents and the temperature field. Finally, section 5 contains a discussion of some of the main findings and gives some conclusions. In particular, it is suggested on the basis of the previously described diagnostic calculations that the cause of the double-peak structure is the latitudinal structure in radiative heating arising from the latitudinal structure in ozone concentrations. This hypothesis is not validated here, but it motivates a further more-detailed dynamical

investigation that is presented in the companion paper (Ming et al. 2016).

2. Data and radiative code

Data are taken from the ERA-Interim dataset (Dee et al. 2011) covering the period from 1991 to 2010. Data are available at a horizontal resolution of 1° and at 6-hourly analysis time intervals (0000, 0600, 1200, and 1800 UTC). We use the data provided on 37 pressure levels for the calculation of dynamical quantities and 60 model levels for the offline radiative calculations. The closest pressure level to 70 hPa in the ERA-Interim output is 66.6 hPa. Where required, the latter level will be used in plots to avoid interpolating the data but referred to as 70 hPa in the text. This does not affect any of the conclusions in this paper. The European Centre for Medium-Range Weather Forecasts (ECMWF) also provides diabatic and physics tendencies from the forecast model used to generate the ERA-Interim dataset, accumulated over 12-h periods with the same horizontal resolution. The diabatic tendencies are provided on 60 model eta (hybrid) levels and are used to compute diabatic heating rates. These are then interpolated to 60 pressure levels, taking account of surface pressure data, to compute zonal averages. The zonal wind tendency (from the physics tendencies) is used in the calculation of the mean residual vertical velocity in section 3.

The structure of the diabatic heating rates is investigated using shortwave and longwave offline radiative codes. The shortwave scheme in ERA-Interim is based on a two-stream method by Fouquart and Bonnel (1980). For the offline clear-sky shortwave (SW) calculations, we instead use the Zhong and Haigh shortwave code (Zhong and Haigh 1995). A three-point Gaussian quadrature method is used to account for the diurnal variation in the solar zenith angle. The albedo is taken from ERA-Interim data.

For the longwave (LW) calculations, ERA-Interim makes use of the Rapid Radiative Transfer Model—Long Wave (RRTMG LW) (Morcrette et al. 2001). In the offline longwave analysis, we make use of the standalone RRTM, version 3.3, longwave code (Mlawer et al. 1997). RRTM employs a correlated-k approach to calculate the heating rates where the k coefficients are obtained directly from a line-by-line code (LBLRRTM). The main difference between RRTM LW (the code used in this paper) and RRTMG LW (the code used by ECMWF) is that RRTMG uses a reduced set of intervals (140) for the integration of absorption in spectral space in each band relative to full set of intervals (256) used in RRTM LW.

Within the ERA-Interim calculation, the radiative code uses an imposed Fortuin and Langematz (1994) ozone climatology (https://www.repository.cam.ac.uk/handle/1810/253669) and the water vapor field that is calculated through the assimilation process. For the offline calculation with the Zhong and Haigh SW code and the RRTM LW code, we therefore provide as input the Fortuin and Langematz (1994) ozone climatology and ERA-Interim water vapor and temperature. The carbon dioxide mixing ratio everywhere is set to 370 ppmv, which is an approximate value appropriate for the year 2000. ERA-Interim assumes carbon dioxide is well mixed and that it is linearly increasing from the 1990 values. The input fields to the radiation code are provided on pressure levels corresponding to the 60 model levels used by the ECMWF model and at every 5° of latitude. Ozone from the monthly Fortuin and Langematz (1994) climatology is linearly interpolated to these pressures and latitudes and also to daily values. A constant surface emissivity of 0.99 is used and the surface temperature is set to the skin temperature from ERA-Interim.

3. Latitudinal structure in upwelling and angular momentum balance

In this section we will demonstrate that there are two local maxima in the upwelling in the tropics at 70 hPa and that these features are consistent with the angular momentum balance. We make use of the downward control approach (Haynes et al. 1991) with careful treatment of the region close to the equator.

In the transformed Eulerian-mean framework (e.g., Andrews et al. 1987) the components of the residual circulation ($\overline{v}^*$, $\overline{w}^*$) are defined through

$$\overline{v}^* = \overline{v} - \frac{1}{\rho_0}\left(\rho_0 \frac{\overline{v'\theta'}}{\overline{\theta}_z}\right)_z = -\frac{\psi^*_z}{\rho_0 \cos\phi}, \tag{1a}$$

$$\overline{w}^* = \overline{w} + \frac{1}{a\cos\phi}\left(\cos\phi \frac{\overline{v'\theta'}}{\overline{\theta}_z}\right)_\phi = \frac{\psi^*_\phi}{a\rho_0 \cos\phi}, \tag{1b}$$

where v and w are the meridional and vertical components of the velocity, respectively, a is the radius of Earth, ϕ is latitude, z is log-pressure height, $\rho_0 \propto \exp(-z/H)$ (H is a scale height taken to be 7 km), θ is the potential temperature, and ψ^* is the residual mass streamfunction. An overbar represents a zonal mean and a prime represents deviation from the zonal mean.

Figure 1a shows different measures of the upwelling at 70 hPa calculated from ERA-Interim fields. The solid line shows the mean residual vertical velocity $\overline{w}^*$ calculated from the meridional velocity and temperature

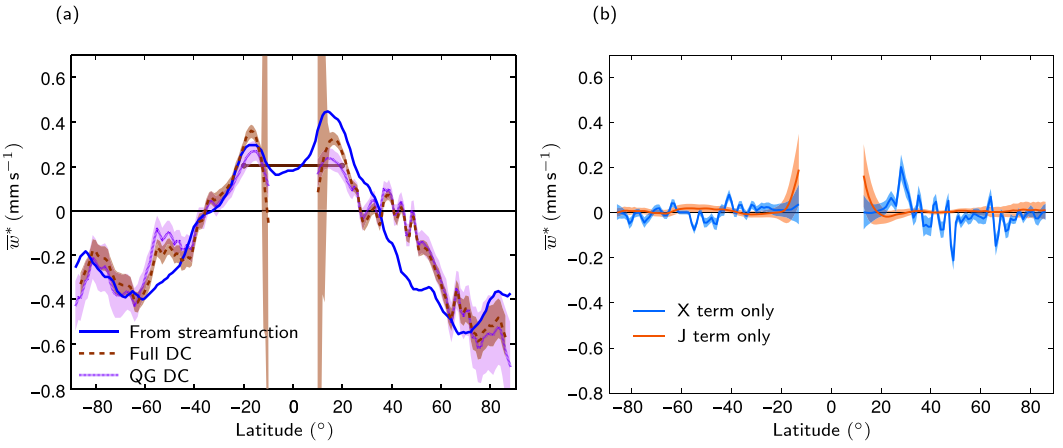

FIG. 2. (a) Plot of the mean vertical residual velocity (mm s^{-1}) at 66.6 hPa, averaged between 1991 and 2010, from ERA-Interim calculated directly from the streamfunction (as in Fig. 1) and from the Eliassen–Palm fluxes using the full expression in (2) for downward control (DC) integral and its quasigeostrophic (QG) approximation in (3). For the last two lines, 95% confidence intervals are calculated from an adjusted Student's t test. The uncertainty diverges for the full downward control case as the meridional gradient in angular momentum becomes small. The horizontal line between 20°N and 20°S represents the mean value of the upwelling in this region obtained using the residual streamfunction calculated for the full downward control case and imposing the fact that the global average of upwelling is zero. (b) As in the full downward control calculation in (a), but only showing the contribution from the unresolved processes X and the interaction between the transient parts of the meridional circulation and the angular momentum J.

following the same method as Seviour et al. (2012). Equation (1a) is used to calculate $\overline{v}^*$ from v and θ. The residual mass streamfunction ψ^* is computed from the pressure integral $\psi^* = \int_0^p \overline{v}^* \, dp'$. Component $\overline{w}^*$ is then obtained from ψ^*. This method means that the ERA-Interim-supplied $\overline{w}$ does not enter the computation and $\overline{w}^*$ is obtained through mass balance from $\overline{v}^*$. This is done since w is less tightly constrained to observations by the data assimilation than v and θ (Monge-Sanz et al. 2013).

The calculated $\overline{w}^*$ is in good agreement with that shown by Seviour et al. (2012) (their calculation is over a slightly different time period: 1989–2009). The dashed line shows the upwelling inferred from the total diabatic heating rates; that is, the "diabatic mean residual vertical velocity" defined by (8) of Butchart (2014). This calculation is intended as a simple estimate of the upwelling from the diabatic heating and we do not impose the constraint that the globally averaged upwelling is zero. The diabatic heating field is linearly interpolated from the 60 model levels to the 66.6 hPa for this calculation. Both methods of calculating the mean residual vertical velocity show that there are two local maxima in the upwelling at 70 hPa centered around 20°N and 20°S. A 95% confidence interval for the estimated $\overline{w}^*$ is also shown as a shaded region using an adjusted Student's t test (Zwiers and von Storch 1995) as described in the appendix.

A corresponding structure is seen in the ERA-Interim zonal-mean diabatic heating rates themselves. Figure 1b shows the total diabatic heating rate plotted as a difference from the equatorial value (this is helpful in emphasizing latitudinal variations, particularly for quantities that have a large vertical gradient). The latitudinal structure in the heating rates is also present in other reanalysis datasets such as the Modern-Era Retrospective Analysis for Research and Applications (MERRA) dataset and the Climate Forecast System Reanalysis (CFSR) but with less-pronounced peaks (Wright and Fueglistaler 2013). The structure and magnitude of the peaks varies with seasons and with the phase of the quasi-biennial oscillation (QBO) (Fueglistaler et al. 2009, their Fig. 8b), but they are present year-round in the multiyear average and are not simply associated with a particular phase of the seasonal cycle or of the QBO.

To consider the consistency of the angular momentum balance, we can make use of the downward control principle (Haynes et al. 1991) to calculate the upwelling from the divergence of the Eliassen–Palm flux ($\nabla \cdot \mathbf{F}$) in ERA-Interim (Fig. 2) ($\nabla \cdot \mathbf{F}$ is calculated from the dynamical fields and therefore represents the effects of the resolved waves). The full downward control integral is

$$\overline{w}^*(z) = \frac{1}{a\rho_0 \cos\phi} \frac{\partial}{\partial \phi} \left[\int_z^\infty \frac{a \cos\phi (\nabla \cdot \mathbf{F})}{\overline{m}_\phi} \bigg|_{\overline{m}} dz_1 \right], \qquad (2)$$

with the integral performed along angular momentum contours. The angular momentum per unit mass is given

by $\overline{m} = a\cos\phi(\overline{u} + a\Omega\cos\phi)$, where u is the zonal wind and Ω is the angular velocity of Earth.

In the extratropics, the angular momentum contours are nearly vertical and it is convenient to calculate the integral at a constant latitude assuming the quasi–geostrophic (QG) limit ($|\overline{u}| \ll 2\Omega a|\sin\phi|$) and hence $\overline{m}_\phi \simeq -2\Omega a^2 \sin\phi\cos\phi$. The downward control integral can then be written in the form

$$\overline{w}^*(z) \simeq \frac{1}{a\rho_0\cos\phi}\frac{\partial}{\partial\phi}\left(\int_z^\infty \frac{\nabla\cdot\mathbf{F}}{2a\Omega\sin\phi}\bigg|_\phi dz_1\right). \qquad (3)$$

Figure 2a shows the upwelling calculated using both the full integral in (2) and the QG approximation in (3). The uncertainty shown relates to the variability present in the 20-yr dataset. The QG and full calculations are essentially indistinguishable in the region poleward of 25°N and 25°S. In the tropics, the contribution of the relative angular momentum to $\overline{m}_\phi$ is not negligible and affects the value of upwelling computed. The full integral in (2) produces an upwelling that is about 0.1 mm s^{-1} larger at the location of the double peaks. The uncertainty in the full downward control integral is large close to the equator since the meridional gradient of the angular momentum $\overline{m}_\phi$ becomes small and strong serial correlations in the data from the annual cycle and quasi-biennial oscillation result in a small number of statistical degrees of freedom in the 20-yr dataset used. However, the peaks in the Northern and Southern Hemispheres are both resolved to within statistical uncertainty in this calculation. Figure 2a also shows the mean value of the upwelling in the region 20°N–S calculated by imposing the constraint that the global-mean upwelling averages to zero on each pressure level. The average in this region is less that the value of either peak, clearly showing that, notwithstanding the absence of reliable estimates from the downward control calculation of the detailed latitudinal structure of the upwelling, the upwelling velocity must be smaller in the tropical region between the two identified peaks and hence two maxima must be present.

Scott (2002) showed that the interaction between the transient parts of the meridional circulation and the angular momentum gives rise to a set of additional terms which can play a role in the time-averaged angular momentum budget. The term $\nabla\cdot\mathbf{F}$ in the numerator of the integral in (2) can be modified to $\nabla\cdot\mathbf{F} + \rho_0 Ja\cos\phi$, where $J = -\langle\overline{v^{*\star}}\partial_\phi\overline{u}^\star/a\rangle - \langle\overline{w^{*\star}}\partial_z\overline{u}^\star\rangle$. Angle brackets denote time averages and stars denote the deviations from the time average. The contribution from J appears to enhance the double peaks but is not essential for their existence (Fig. 2b).

In models there is often a significant contribution to the angular momentum budget from parameterized processes (e.g., Butchart et al. 2011). ERA-Interim also provides a zonal wind tendency field that is the momentum forcing due to parameterized processes (including gravity wave drag). The tendency represents a force on the atmosphere and the part associated with gravity waves may be included in $\nabla\cdot\mathbf{F}$ in (2). Figure 2b shows the contribution of this term to the upwelling. The zonal wind tendencies are provided on 60 model levels and linearly interpolated to the same 37 pressure levels used in the previous full downward control calculations. In the region of interest, this term does not change the upwelling calculated to within the uncertainty in the calculations.

In summary, the double peak in upwelling is consistent with the structure of the resolved wave forcing in ERA-Interim data with little evidence for a significant role for parameterized waves.

4. Origin of the diabatic heating structures at 70 hPa

As noted previously, there is a double-peak structure in the diabatic heating rates corresponding to those in the upwelling. Using offline radiative calculations, we will consider in this section how the double-peak structure in the heating arises and to what extent it can be regarded as externally imposed. The difference between the total ERA-Interim diabatic heating rate and the equatorial value has been shown in Fig. 1b. Figure 3a shows the corresponding field without subtracting the equatorial value. The double-peak structure at about 70 hPa with maxima centered around 20°N/S is clear. ERA-Interim also provides individual radiative components of the diabatic heating. These include a clear-sky (radiative transfer without clouds) heating and an all-sky (with clouds) heating, each further divided into shortwave (SW) and LW radiation contributions. The nonradiative components, which represent a combination of latent heating and diffusive and turbulent heat transport, can be computed as a residual (Fueglistaler et al. 2009). The total contribution from radiative processes is shown in Fig. 3b, which is composed of the clear-sky shortwave (Fig. 3c), the clear-sky longwave (Fig. 3d), and the net heating (LW and SW) from clouds (Fig. 3e). Figure 3f shows the nonradiative components.

The contribution of the different components of the diabatic heating to the double-peak structure is summarized in Fig. 4 by showing, for each component, the difference between 20°N and the equator as a function of height. At 70 hPa, there is a 0.29 K day^{-1} difference in the heating between 20°N and the equator, of which 0.18 K day^{-1} is due to the clear-sky longwave, 0.06 K day^{-1} is due to the clear-sky shortwave, 0.02 K day^{-1} is from

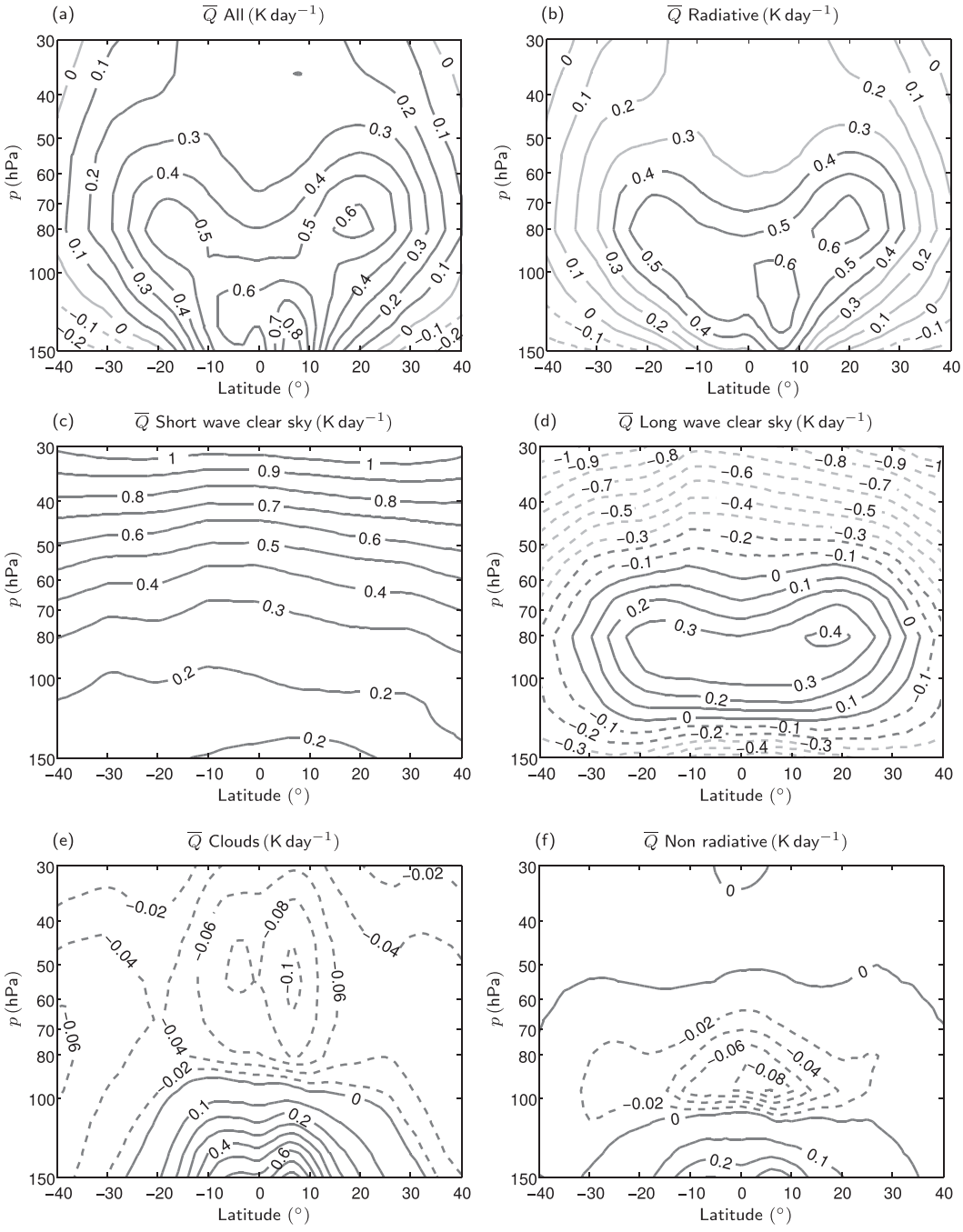

FIG. 3. Zonal-mean diabatic heating rates (K day^{-1}) from ERA-Interim averaged between 1991 and 2010. (a) Total diabatic heating rate. (b) All-sky diabatic heating rate from radiative processes [equal to the sum of (c),(d), and (e)]. (c) Clear-sky shortwave heating rate. (d) Clear-sky longwave heating rate. (e) Radiative contribution from clouds (both in LW and SW). (f) Nonradiative diabatic processes calculated as a residual [(a) minus (b)]. Contour intervals are 0.1 K day^{-1} with additional contours at 0.02 K day^{-1} for the negative values in (e) and (f).

the cloud effect, and the remainder is from nonradiative effects.

The radiative effect of clouds on the lower stratosphere (Fig. 3e) is essentially that optically thick clouds in the upper troposphere suppress the upwelling longwave radiation and hence reduce longwave heating due to ozone absorption in the lower stratosphere (Doherty et al. 1984; Hartmann et al. 2001; Gettelman et al. 2004). The reduced longwave heating effect of clouds in the lower stratosphere is largest close to the

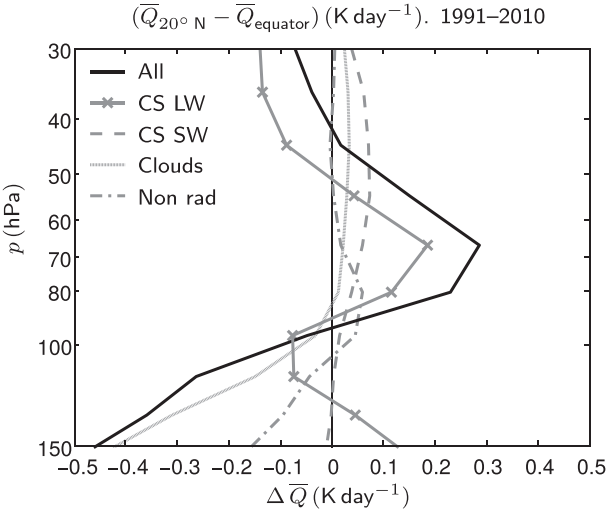

FIG. 4. Difference between the zonal-mean diabatic heating rates (K day^{-1}) at 20°N and the equator from ERA-Interim averaged over the years 1991–2010.

equator and hence acts to increase the latitudinal gradients away from the equator in the double-peak structure. Nonradiative diabatic effects, shown in Fig. 3f, are important near the tropopause. Although their contribution decreases rapidly with height above 90 hPa, they lead to a relative cooling at 70 hPa over the equator of a magnitude similar to the cloud effect.

We will now discuss the clear-sky shortwave and longwave contributions in more detail with offline radiative calculations. The following analysis compares 20°N and equator. We also compare 20°S and the equator. While the peak in diabatic heating at 20°S is smaller than in the Northern Hemisphere, the qualitative aspects of the contributions are the same and these results are not shown.

a. Clear-sky shortwave

Figure 3c shows the SW clear-sky contribution in ERA-Interim. There is a strong increase with height but also a latitudinally varying part that increases away from the equator and hence contributes to the double-peak structure. These features are reproduced by the offline calculation with the Zhong and Haigh radiative code, results of which are shown in Fig. 5a. Water vapor and temperature fields from ERA-Interim are zonally averaged and an annually varying climatology is produced using the data from 1991 to 2010. The Fortuin and Langematz (1994) zonal-mean ozone climatology is provided as monthly means and is linearly interpolated to daily values. The radiative calculation is done daily and the heating rates are then time averaged. There are small differences between the offline calculation (Fig. 5a) and the ERA-Interim values (Fig. 3c) of about 0.01 K day^{-1} at 70 hPa, which are likely to be due to differences in the radiation code and the use of a zonally averaged climatology.

Figure 5b shows the difference in the heating rate between 20°N and the equator according to the offline calculation (solid black line) and according to ERA-Interim (dashed gray curve). There is a contribution of about 0.07 K day^{-1} at 70 hPa to the total diabatic heating shown in Fig. 1b. This contribution is primarily due to the latitudinal gradient in ozone evident in Figs. 5c and 5d. This ozone gradient is also present in more recent climatologies such as the Halogen Occultation Experiment (HALOE; Grooß and Russell 2005) and the multi-instrument mean of satellite data (Tegtmeier et al. 2013). The offline radiative calculation is repeated at 20°N with the ozone profile held fixed at the equatorial value and the difference between the calculated clear-sky shortwave heating at 20°N and the equator is shown as the dashed–dotted line. This difference therefore results primarily from the latitudinal variation in incident shortwave radiation and, as can be seen, it is negligible. Hence, the latitudinal gradient in ozone plays the dominant role in determining the latitudinal gradient in the clear-sky shortwave heating rates.

b. Clear-sky longwave

Since from the above it appears that the clear-sky longwave component is a large contributor to the overall double-peak structure in the heating, we now analyze this component further to establish how it arises from the distribution of temperature and trace-gas concentrations using the RRTM radiation code as described in section 2.

We will first demonstrate that it is possible to reproduce the double-peak structure seen in the longwave clear-sky radiative heating rates in ERA-Interim using RRTM. A single year (2000) is chosen to allow a comprehensive approach where the radiative calculation is carried out daily.

Figures 6a and 6b compares the zonally averaged clear-sky longwave heating rate for the year 2000 from ERA-Interim and the offline RRTM calculation. Both are plotted as differences from the equatorial value. The offline calculation shows that it is possible to reproduce the double-peak structure in the LW heating with good agreement with the ERA-Interim values. Further radiative calculations show that the contributions to the heating rates in this region from nitrous oxide, methane, CFC-11, and CFC-12, as prescribed in ERA-Interim, are negligible. Background stratospheric aerosols were not included, but their radiative impact, estimated using results reported by Ramachandran et al.

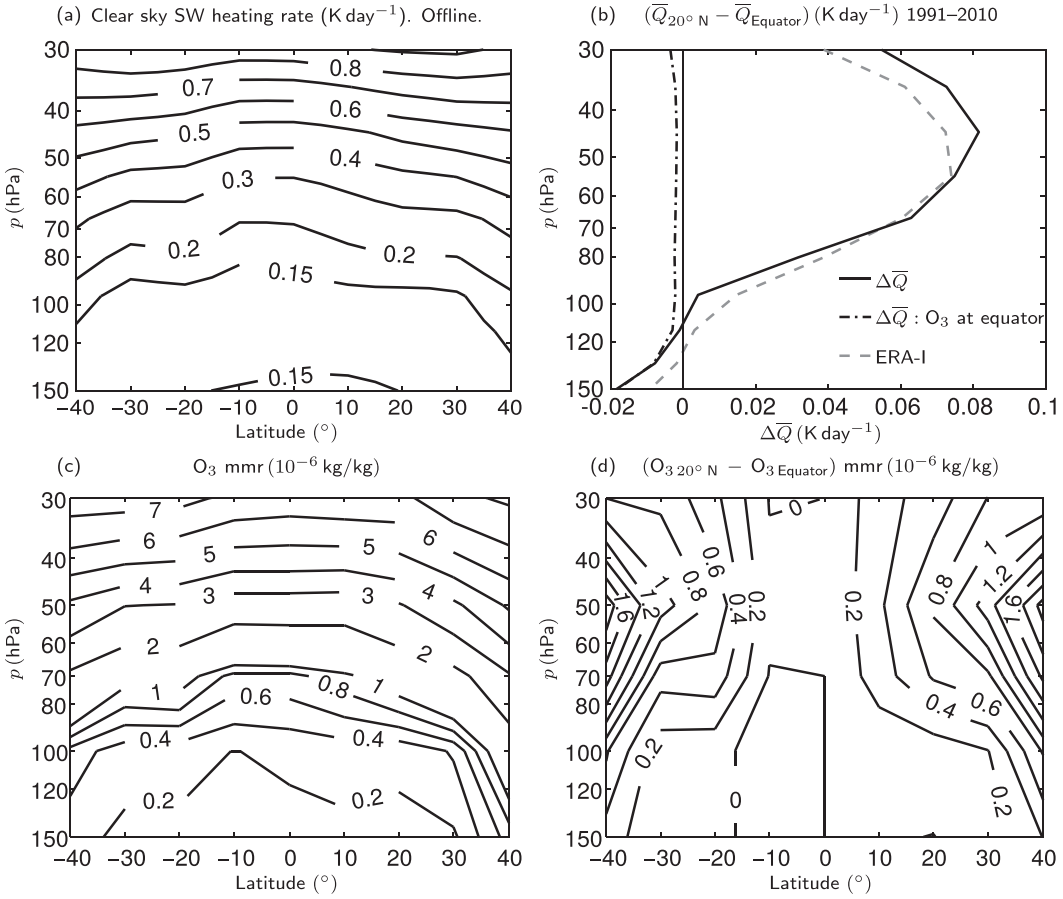

FIG. 5. (a) Zonal-mean clear-sky shortwave heating rates (K day^{-1}) obtained from an offline calculation with the Zhong and Haigh (1995) radiation code. (b) Difference between the zonal-mean diabatic heating rates at 20°N and the equator. The solid black line uses the same data as in (a). For the dashed–dotted black line, ozone is kept at the values at the equator. The dashed gray line shows the ERA-Interim clear-sky shortwave heating rates (same data as in Fig. 3c). (c) Zonal- and time-mean Fortuin and Langematz (1994) ozone climatology. (d) As in (c), but shown as a difference from the ozone mixing ratio at the equator to emphasize the meridional gradient.

(2000), suggests that the diabatic heating rate contribution in the region of the double peak in heating is an order of magnitude smaller. The major trace gases—carbon dioxide, ozone, and water vapor—are responsible for most of the double-peak structure.

To understand how the structure of the double peak in clear-sky longwave heating arises in the climatological mean, we run a set of one-dimensional radiative calculations with ERA-Interim water vapor and temperature data that is zonally and time averaged (1991–2010) and with the annual-mean Fortuin and Langematz (1994) ozone. The profiles of temperature and ozone are used to produce the clear-sky longwave heating rate at the equator and at 20°N.

Time- and zonally averaged profiles were used for economy. The difference between the heating rates at the equator and at 20°N in the time- and zonally averaged calculation, which is the primary interest here, is in very good agreement (to within ~0.02 K day^{-1}) with the difference taken directly from the ERA-Interim heating rates. A more detailed calculation for the year 2000 was performed, as a check, where the rates were calculated independently at 12 longitudes and daily before being averaged. This calculation confirmed that using the time- and zonally averaged profiles for the difference does not affect the conclusions in this paper.

The calculation is repeated using the ozone profile from 20°N while keeping the equatorial water vapor and temperature profiles. The mixing ratio for carbon dioxide and other trace gases is the same as in the previous calculation. The difference between these two calculations is shown in Fig. 7 by curve A and represents the contribution of the latitudinal ozone difference between 20°N and the equator to the difference in heating rate. The contributions of the latitudinal differences in water vapor and in temperature are indicated by curves B and

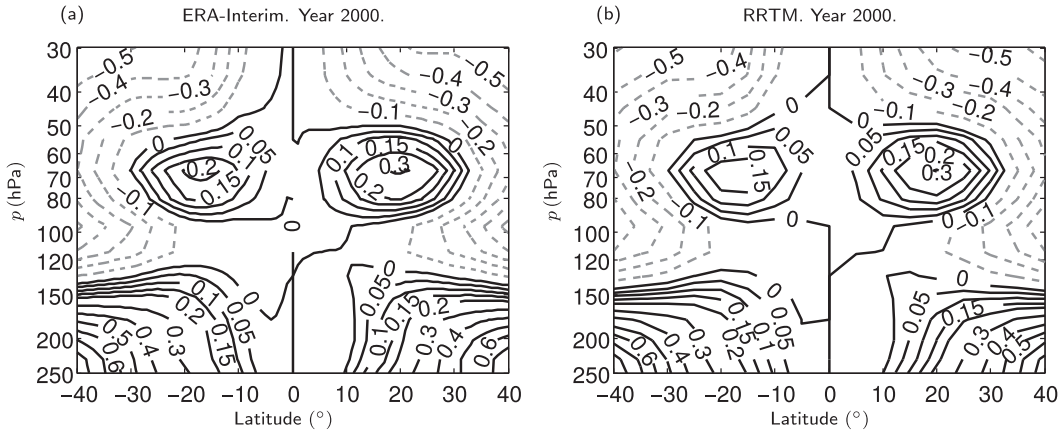

FIG. 6. Zonal-mean longwave clear-sky diabatic heating rates for the year 2000 (a) from ERA-Interim (output produced every 3 h) and (b) using the RRTM radiation code, using the Fortuin and Langematz (1994) ozone climatology, daily values of water vapor and temperature from ERA-Interim, and a CO_2 mixing ratio of 370 ppmv. More details can be found in the main text. Contour intervals are 0.1 K day^{-1} with additional contours at 0.05 and 0.15 K day^{-1}.

C, calculated in a similar way to curve A but with water vapor and temperature individually being changed rather than ozone. The solid black line shows the difference in heating between 20°N and the equator using trace-gas concentrations at their respective latitudes. We also show the ERA-Interim clear-sky longwave heating rate (similar to Fig. 4). The sum of the three contributions (see curve A+B+C) adds linearly to the total difference. The effect of overlapping spectral bands (Clough and Iacono 1995) therefore appears too small in this region.

At 70 hPa, the latitudinal difference in heating rate is 0.18 K day^{-1} of which 0.13 K day^{-1} comes from the latitudinal difference in ozone. The contribution from the latitudinal difference in temperature is 0.04 K day^{-1} and the remainder comes from water vapor. The ozone contribution arises from the fact that, in the tropical lower stratosphere, around 70 hPa, there are larger ozone mixing ratios (Figs. 5c and 5d) and hence more effective absorption of upwelling longwave radiation off the equator than on it. The radiative calculation also shows that the water vapor contribution in the region of interest is of secondary importance.

The latitudinal temperature difference leads to a relative heating in the longwave at 70 hPa, notwithstanding the fact that at this level, as noted previously, temperatures are higher at 20°N than on the equator (Fig. 1c). The explanation is provided by the vertical nonlocality of the dependence of heating rate on temperature. Figure 8 shows the contribution to the difference between 20°N and the equator in clear-sky longwave heating rate at 70 hPa from the corresponding temperature at each of the individual pressure levels. Ozone and water vapor profiles are held at their equatorial values and radiative calculations carried out at the equator with the temperature at individual pressure levels perturbed to the value at 20°N. The contribution

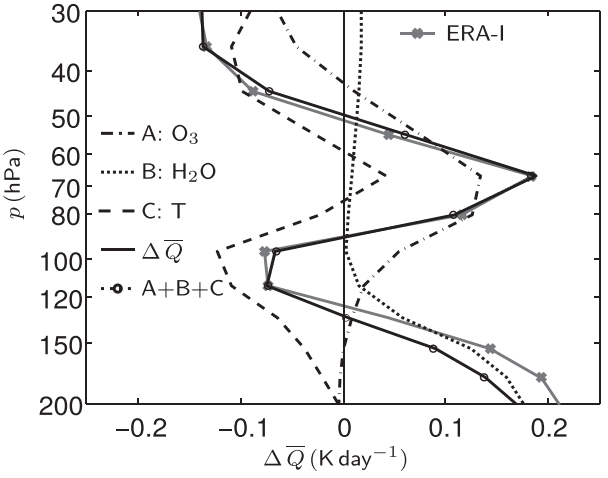

FIG. 7. Radiative calculations using the RRTM LW code to show the effect of the meridional gradients in temperature and ozone between the equator and 20°N on the longwave heating rate. Profiles of temperature, ozone, and water vapor input into the radiation code are averaged zonally and between 1991 and 2010. Curve A is the difference in longwave heating rate calculated at the equator from using the ozone profile at 20°N with water vapor and temperature held at equatorial values. Curves B and C are similar to A, but for the water vapor and temperature meridional gradients, respectively. The solid line labeled ΔQ is the difference in heating calculated at 20°N and the equator using the trace-gas concentrations and temperatures at their respective latitudes. For reference, the plot of the clear-sky longwave heating-rate difference from ERA-Interim, from Fig. 4, is repeated (solid gray line with crosses). Note that the curve for ΔQ (solid black) overlaps curve A+B+C (dashed with circles).

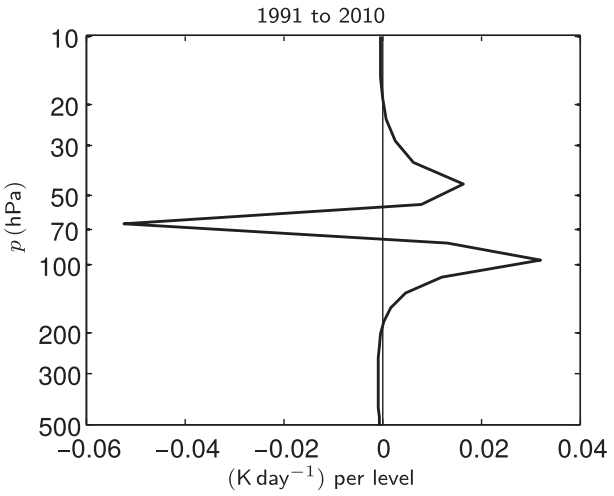

FIG. 8. The contribution to the clear-sky longwave heating rates at 70 hPa arising from the temperature difference between 20°N and the equator at each of the individual pressure levels. The calculation uses the RRTM LW code with ERA-Interim data averaged from 1991 to 2010.

to the difference in heating rate per level as a result of this perturbation is then plotted against the pressure level of the perturbation. Again, the individual contributions are additive; that is, the sum of the heating rate changes due to all pressure levels as shown by the solid curve is equal to the total contribution from temperature to the clear-sky longwave heating at 70 hPa. The solid curve shows that the positive contribution from the latitudinal difference in temperature to the latitudinal difference in heating at 70 hPa comes from layers above and below 70 hPa, which compensate for the local negative effect from the latitudinal difference in temperature at 70 hPa itself. The nonlocal temperature effect, particularly in the region below 100 hPa, might be expected to be decoupled from the dynamical processes around 70 hPa and therefore acts as an external (longwave) radiative forcing at that level.

The longwave heating rates in this region are quite sensitive to the choice of ozone climatology. Similar calculations carried out with the Fortuin and Kelder (1998) climatology, which has about a 20% lower difference in ozone values between 20°N and the equator yielded net heating-rate differences of 0.05 K day^{-1} smaller than those found with the Fortuin and Langematz (1994) climatology used by ERA-Interim. We note in passing that several recent papers have pointed out differences in radiative heating in this region of a similar order between various modern reanalysis products (Wright and Fueglistaler 2013; Randel and Jensen 2013). These biases may well be related to the representation of ozone in each given reanalysis given that differences in the respective ozone fields (Wright and Fueglistaler 2013, their Fig. 1) are of a similar magnitude to those between the Fortuin and Langematz (1994) and the Fortuin and Kelder (1998) climatologies.

We have now demonstrated that the double-peak structure in the heating arises from the structure in the constituents and temperature field. Ozone is the largest contributor to the latitudinal structure.

5. Discussion

In this paper we have examined the double-peak structure in the low-latitude lower stratosphere seen in the ERA-Interim dataset in both diabatic heating (Fueglistaler et al. 2009) and correspondingly in the upwelling vertical velocity (Seviour et al. 2012) and also in reanalyses and model simulations. The upwelling was shown, using the downward control integral, to be consistent with that inferred from the resolved wave force. We examined the various contributions to diabatic heating in detail using an offline radiative code and showed that the double-peak structure in the heating is caused primarily by the latitudinal structure in ozone, with smaller contributions from the structure in temperature and in other radiative constituents. The ozone variation gives rise to a corresponding variation in heating due to both the longwave and shortwave absorption. For the clear-sky longwave heating rates, ~70% of the difference between 20°N and the equator at 70 hPa averaged over 1991–2010 can be attributed to the ozone meridional gradient and ~20% can be attributed to the meridional gradients in temperature throughout the vertical, with the latter coming from the latitudinal variations in temperature in the atmospheric layers below and above the level of the double peak. The latitudinal variation of temperature at 70 hPa itself acts, if anything, to reduce the double peak.

As we have noted previously, the double peak in heating in ERA-Interim is present year-round but the size of the peak compared to the value at the equator is modulated by an annual cycle and by interannual variations such as the QBO (Fueglistaler et al. 2009). Correspondingly, there is a significant interannual variability in the temperature contribution to the double peak. Interannual variability in the ozone contribution is also likely to be important but has not been considered in this study.

These findings motivate the hypothesis that the double peak in heating and, by extension, the double peak in upwelling, which is largely confined to the 90–60-hPa layer, is forced by aspects of radiative heating that are external to the temperature structure and indeed the

dynamics of that layer. In particular, ozone concentrations within that layer and the temperature structure in the layers above, in the middle stratosphere, and below, in the upper troposphere, are important. This hypothesis is consistent with the structure in the temperature field, which does not show a double peak and is relatively flat across latitudes. The alternative hypothesis would have been that the latitudinal structure in upwelling was due to a dynamically determined (e.g., by wave dynamics) structure in the wave force in the absence of any latitudinal structure in the external radiative forcing. The structure of the temperature field would then correspond to that of the upwelling, which is not the case.

The question of what, within a given configuration of the circulation, can be regarded as externally imposed is, of course, a subtle one. While from a purely dynamical point of view the ozone concentration field, and hence any radiative effects arising from it, might be regarded as externally imposed, that would not be the case in a ''chemistry–circulation'' point of view in which dynamics, chemistry, and transport of radiatively active species and radiative heating are all coupled. However, as is evident from Figs. 5c and 5d, the double peak in ozone longwave and shortwave heating arises simply from the fact that, in the lower stratosphere, ozone concentrations increase poleward along pressure surfaces. The explanation for the poleward increase is that, broadly speaking, in the lower stratosphere ozone is a long-lived chemical species with concentration increasing upward and, as for any such species, the action of the Brewer–Dobson circulation on surfaces of constant concentration is to steepen them relative to isentropic surfaces (or other quasi-horizontal surfaces) (e.g., Holton 1986). The poleward increase of ozone concentrations is a rather robust prediction of 2D chemistry-transport models (e.g., Yang et al. 1991) that include the Brewer–Dobson upwelling at low latitudes and downwelling at high latitudes and there is no evidence that it depends on the details of the latitudinal structure (e.g., a double peak) in the Brewer–Dobson vertical velocity. It is also relevant to note that the double peaks in upwelling would, if anything, be likely to lead to ozone concentrations that decrease in latitude away from the equator, rather than increase. Therefore, for the particular case of explaining the double-peak structure, the view that the ozone field is externally imposed seems defensible.

The hypothesis that the double peak in upwelling is caused by the latitudinal structure in the externally imposed part of the radiative heating requires that the change in wave force necessary to maintain angular momentum balance is itself is a response to the imposed heating. The dynamical plausibility of this is demonstrated in the companion paper (Ming et al. 2016).

Acknowledgments. The authors thank Amanda Maycock for help with the radiation code and for helpful discussions. AM and PHi acknowledge funding support from the European Research Council through the ACCI project (Grant 267760) lead by John Pyle. PHi also acknowledges support from an NSERC postdoctoral fellowship. The authors are grateful to Stephan Fueglistaler and Tom Flannaghan for conversations that stimulated some of this work. We also thank Robin Hogan, Alessio Bozzo, and Irina Sandu from ECMWF for their help with reproducing the longwave heating rates, as well as Ulrike Langematz and Markus Kunze for the ozone climatology. We received detailed and helpful comments from three anonymous reviewers that improved this manuscript.

APPENDIX

Statistical Methods

The reanalysis data contain serial correlations that must be taken into account when testing statistical significance and estimating confidence intervals. Consider a time series x with sample size n and sample mean $\overline{x}$. We follow the method described in Zwiers and von Storch (1995), which entails estimating an effective number of degrees of freedom n_e from the autocorrelation function $\rho(t)$ of the time series. Confidence intervals are based on a modified estimate of the standard deviation of the sample mean, $\hat{\sigma}_\mu = \hat{s}\hat{n}_e^{-1/2}$, where $\hat{s}$ is the standard deviation of the time series and

$$\hat{n}_e = \frac{n}{1 + 2\sum_{t=1}^{n-1}(1 - t/n)\rho(t)}. \tag{A1}$$

Adequate convergence of the sum in the denominator in (A1) can be obtained if terms in the autocorrelation function are retained up to the lag where ρ falls below e^{-2}. The distribution of the means is assumed to follow a Student's t distribution with $\hat{n}_e - 1$ degrees of freedom. This method is referred to as the adjusted Student's t test.

A further check on the uncertainty estimates is performed by splitting the dataset into a set of smaller continuous subsamples of length N and means $\hat{m}_i$, where the subscript i denotes a subsample. Two different estimators for the standard deviation of the subsample means $\hat{\sigma}_m(N)$ and $\hat{\sigma}_\mu(N)$ are obtained and compared as N is changed. The first method involves scaling the former with N to give $\hat{\sigma}_\mu(N) = (\hat{n}_e n/N)^{-1/2}\hat{s}$. The second estimate $\hat{\sigma}_m(N)$ is given by the standard deviation of the means $\hat{m}_i$. These estimates should converge if the

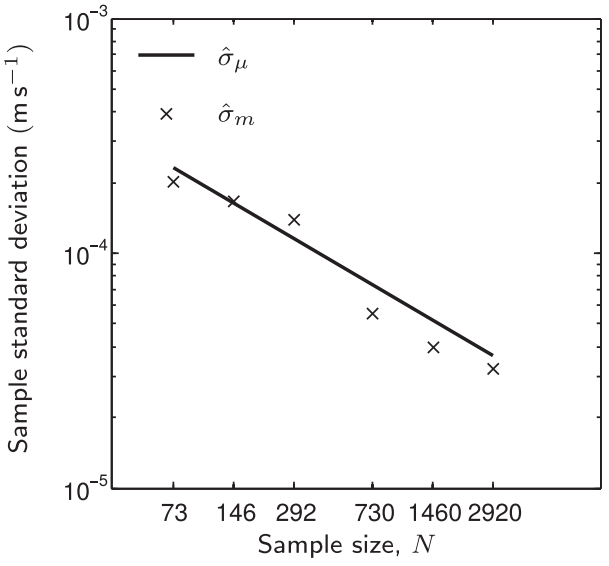

FIG. A1. Estimates of the standard deviation in $\overline{w}^*$ from ERA-Interim at 20°N and 66.6 hPa computed from 6-hourly data from 1991 to 2010 ($n = 29\,200$); $n_e = 4100$.

adjusted standard deviation for the whole time series $\hat{\sigma}_\mu(n)$ is reasonable.

An example of this convergence for $\overline{w}^*$ from ERA-Interim at 20°N and 70 hPa is plotted in Fig. A1, showing good agreement with $n_e \approx 4100$ ($n = 29\,200$).

REFERENCES

Abalos, M., B. Legras, F. Ploeger, and W. J. Randel, 2015: Evaluating the advective Brewer-Dobson circulation in three reanalyses for the period 1979–2012. *J. Geophys. Res. Atmos.*, **120**, 7534–7554, doi:10.1002/2015JD023182.

Andrews, D. G., J. R. Holton, and C. B. Leovy, 1987: *Middle Atmosphere Dynamics.* International Geophysics Series, Vol. 40, Academic Press, 489 pp.

Brewer, A. W., 1949: Evidence for a world circulation provided by the measurements of helium and water vapour distribution in the stratosphere. *Quart. J. Roy. Meteor. Soc.*, **75**, 351–363, doi:10.1002/qj.49707532603.

Butchart, N., 2014: The Brewer-Dobson circulation. *Rev. Geophys.*, **52**, 157–184, doi:10.1002/2013RG000448.

——, and A. A. Scaife, 2001: Removal of chlorofluorocarbons by increased mass exchange between the stratosphere and troposphere in a changing climate. *Nature*, **410**, 799–802, doi:10.1038/35071047.

——, and Coauthors, 2006: Simulations of anthropogenic change in the strength of the Brewer–Dobson circulation. *Climate Dyn.*, **27**, 727–741, doi:10.1007/s00382-006-0162-4.

——, and Coauthors, 2010a: Chemistry–climate model simulations of twenty-first century stratospheric climate and circulation changes. *J. Climate*, **23**, 5349–5374, doi:10.1175/2010JCLI3404.1.

——, and Coauthors, 2010b: Stratospheric dynamics. SPARC CCMVal report on the evaluation of chemistry-climate models, SPARC Rep. 5, WCRP-30/2010, WMO/TD-40, 109–147. [Available online at http://www.sparc-climate.org/publications/sparc-reports/sparc-report-no5/.]

——, and Coauthors, 2011: Multimodel climate and variability of the stratosphere. *J. Geophys. Res.*, **116**, D05102, doi:10.1029/2010JD014995.

Clough, S. A., and M. J. Iacono, 1995: Line-by-line calculation of atmospheric fluxes and cooling rates: 2. Application to carbon dioxide, ozone, methane, nitrous oxide and the halocarbons. *J. Geophys. Res.*, **100**, 16 519–16 535, doi:10.1029/95JD01386.

Dee, D. P., and Coauthors, 2011: The ERA-Interim reanalysis: Configuration and performance of the data assimilation system. *Quart. J. Roy. Meteor. Soc.*, **137**, 553–597, doi:10.1002/qj.828.

Doherty, G. M., R. E. Newell, and E. F. Danielsen, 1984: Radiative heating rates near the stratospheric fountain. *J. Geophys. Res.*, **89**, 1380–1384, doi:10.1029/JD089iD01p01380.

Fortuin, J. P., and U. Langematz, 1994: Update on the global ozone climatology and on concurrent ozone and temperature trends. *Atmospheric Sensing and Modelling*, R. P. Santer, Ed., International Society for Optical Engineering (SPIE Proceedings, Vol. 2311), 207–216, doi:10.1117/12.198578.

——, and H. Kelder, 1998: An ozone climatology based on ozonesonde. *J. Geophys. Res.*, **103**, 31 709–31 734, doi:10.1029/1998JD200008.

Fouquart, Y., and B. Bonnel, 1980: Computations of solar heating of the Earth's atmosphere: A new parameterization. *Beitr. Phys. Atmos.*, **53**, 35–62.

Fueglistaler, S., B. Legras, A. Beljaars, J.-J. Morcrette, A. Simmons, A. M. Tompkins, and S. Uppala, 2009: The diabatic heat budget of the upper troposphere and lower/mid stratosphere in ECMWF reanalyses. *Quart. J. Roy. Meteor. Soc.*, **135**, 21–37, doi:10.1002/qj.361.

Garcia, R. R., and W. J. Randel, 2008: Acceleration of the Brewer–Dobson circulation due to increases in greenhouse gases. *J. Atmos. Sci.*, **65**, 2731–2739, doi:10.1175/2008JAS2712.1.

Gettelman, A., P. M. Forster, M. Fujiwara, Q. Fu, H. Vömel, L. K. Gohar, C. Johanson, and M. Ammerman, 2004: Radiation balance of the tropical tropopause layer. *J. Geophys. Res.*, **109**, D07103, doi:10.1029/2003JD004190.

Grooß, J.-U., and J. Russell III, 2005: Technical note: A stratospheric climatology for O3, H2O, CH4, NOx, HCl and HF derived from HALOE measurements. *Atmos. Chem. Phys.*, **5**, 2797–2807, doi:10.5194/acp-5-2797-2005.

Hartmann, D. L., J. R. Holton, and Q. Fu, 2001: The heat balance of the tropical tropopause, cirrus, and stratospheric dehydration. *Geophys. Res. Lett.*, **28**, 1969–1972, doi:10.1029/2000GL012833.

Haynes, P. H., M. E. McIntyre, T. G. Shepherd, C. J. Marks, and K. P. Shine, 1991: On the "downward control" of extratropical diabatic circulations by eddy-induced mean zonal forces. *J. Atmos. Sci.*, **48**, 651–680, doi:10.1175/1520-0469(1991)048<0651:OTCOED>2.0.CO;2.

Holton, J. R., 1986: Meridional distribution of stratospheric trace constituents. *J. Atmos. Sci.*, **43**, 1238–1242, doi:10.1175/1520-0469(1986)043<1238:MDOSTC>2.0.CO;2.

Ming, A., P. Hitchcock, and P. Haynes, 2016: The response of the lower stratosphere to zonally symmetric thermal and mechanical forcing. *J. Atmos. Sci.*, **73**, 1903–1922, doi:10.1175/JAS-D-15-0294.1.

Mlawer, E. J., S. J. Taubman, P. D. Brown, M. J. Iacono, and S. A. Clough, 1997: Radiative transfer for inhomogeneous atmospheres: RRTM, a validated correlated-k model for the longwave. *J. Geophys. Res.*, **102**, 16 663–16 682, doi:10.1029/97JD00237.

Monge-Sanz, B. M., M. P. Chipperfield, D. P. Dee, A. J. Simmons, and S. M. Uppala, 2013: Improvements in the stratospheric transport achieved by a chemistry transport model with ECMWF (re)analyses: Identifying effects and remaining challenges. *Quart. J. Roy. Meteor. Soc.*, **139**, 654–673, doi:10.1002/qj.1996.

Morcrette, J.-J., E. J. Mlawer, M. J. Iacono, and S. A. Clough, 2001: Changes to the Operational Forecasting System. *ECMWF Newsletter*, No. 91, ECMWF, Reading, United Kingdom, 1–2.

Plumb, R. A., 2002: Stratospheric transport. *J. Meteor. Soc. Japan*, **80**, 793–809, doi:10.2151/jmsj.80.793.

Ramachandran, S., V. Ramaswamy, G. L. Stenchikov, and A. Robock, 2000: Radiative impact of the Mount Pinatubo volcanic eruption: Lower stratospheric response. *J. Geophys. Res.*, **105**, 24 409–24 429, doi:10.1029/2000JD900355.

Randel, W. J., and E. J. Jensen, 2013: Physical processes in the tropical tropopause layer and their roles in a changing climate. *Nat. Geosci.*, **6**, 169–176, doi:10.1038/ngeo1733.

Scott, R. K., 2002: Wave-driven mean tropical upwelling in the lower stratosphere. *J. Atmos. Sci.*, **59**, 2745–2759, doi:10.1175/1520-0469(2002)059<2745:WDMTUI>2.0.CO;2.

Seviour, W. J. M., N. Butchart, and S. C. Hardiman, 2012: The Brewer–Dobson circulation inferred from ERA-Interim. *Quart. J. Roy. Meteor. Soc.*, **138**, 878–888, doi:10.1002/qj.966.

Shepherd, T. G., and C. McLandress, 2011: A robust mechanism for strengthening of the Brewer–Dobson circulation in response to climate change: Critical-layer control of subtropical wave breaking. *J. Atmos. Sci.*, **68**, 784–797, doi:10.1175/2010JAS3608.1.

Tegtmeier, S., and Coauthors, 2013: SPARC Data Initiative: A comparison of ozone climatologies from international satellite limb sounders. *J. Geophys. Res. Atmos.*, **118**, 12 229–12 247, doi:10.1002/2013JD019877.

Wright, J. S., and S. Fueglistaler, 2013: Large differences in reanalyses of diabatic heating in the tropical upper troposphere and lower stratosphere. *Atmos. Chem. Phys.*, **13**, 9565–9576, doi:10.5194/acp-13-9565-2013.

Yang, H., E. Olaguer, and K. K. Tung, 1991: Simulation of the present-day atmospheric ozone, odd nitrogen, chlorine and other species using a coupled 2-D model in isentropic coordinates. *J. Atmos. Sci.*, **48**, 442–471, doi:10.1175/1520-0469(1991)048<0442:SOTPDA>2.0.CO;2.

Zhong, W., and J. D. Haigh, 1995: Improved broadband emissivity parameterization for water vapor cooling rate calculations. *J. Atmos. Sci.*, **52**, 124–138, doi:10.1175/1520-0469(1995)052<0124:IBEPFW>2.0.CO;2.

Zwiers, F. W., and H. von Storch, 1995: Taking serial correlation into account in tests of the mean. *J. Climate*, **8**, 336–351, doi:10.1175/1520-0442(1995)008<0336:TSCIAI>2.0.CO;2.